Active rod accumulation in microchannels with elliptic cross-section

Crioni Love Cuenca, Mykhailo Potomkin

1 Introduction

An active rod is a model for particles capable of converting free energy into persistent motion [1], particularly biological and bio-mimetic micro-swimmers such as bacteria or bimetallic microrods. Despite its simplicity, the active rod model exhibits a number of self-organized, collective phenomena including wall accumulation, upstream motion, formation of moving polar clusters, among others [1, 4]. These developments not only shed light on the field of biological self-organization, but additionally open doors to applications in medicine and materials science [5], more of which will be discussed in section four of this report. That being said, previous studies have considered these rods in trapezoid confinements in order to describe the physical and geometric dependence of their focusing [4], and in another case have found that within boundaries (e.g., nozzles and channels) the majority of active rods self-align in areas with high shear [5]. Altogether, we find that introducing a confinement reveals a rich variety of characteristics among active rods.

In this project, we investigate how active rod accumulation depends on the curvature of its confinement by considering confinements of varying curvature, which we later combine with various physical parameters. In other words, our goal is to determine whether or not it is possible to control active rod location via the confinement curvature. To this end, active rods will be simulated in a straight channel with the elliptic cross section. Because rods are accumulated uniformly along the confinement when the cross-section is a circle, we will consider an aspect ratio not equal to 1, indicating that there are two side points where the curvature is maximal. We hypothesize that rods will tend to accumulate at these points and will test our theory via numerical simulations implemented in MATLAB.

2 Model

We begin this study by deriving equations modeling an active rod in $\mathbb{R}^3$. We introduce the orthonormal basis $(p(t), e_\theta(t), e_\varphi(t))$,

$$
p(t) = \begin{bmatrix} \cos\varphi(t)\sin\theta(t) \\ \sin\varphi(t)\sin\theta(t) \\ \cos\theta(t) \end{bmatrix}, \; e_\theta = \begin{bmatrix} \cos\varphi(t)\cos\theta(t) \\ \sin\varphi(t)\cos\theta(t) \\ -\sin\theta(t) \end{bmatrix}, \; e_\varphi = \begin{bmatrix} -\sin\varphi(t) \\ \cos\varphi(t) \\ 0 \end{bmatrix},
$$

where p is the unit orientation vector, e_θ and e_φ are the unit basis vectors for the spherical coordinates, and $0 \le \theta(t) \le \pi$ and $-\pi < \varphi(t) \le \pi$ are the direction angles of the active rod.

Moreover, we will consider the background flow u_{BG} along the z axis, such that $u = v = 0$ and $w = w(x,y) = x^2 + 2y^2 - 1$. Then,

$$u_{\text{BG}}(x,y,z) = \begin{bmatrix} u(x,y,z) \\ v(x,y,z) \\ w(x,y,z) \end{bmatrix} \quad \text{and} \quad \nabla u = \begin{bmatrix} \partial_x u & \partial_y u & \partial_z u \\ \partial_x v & \partial_y v & \partial_z v \\ \partial_x w & \partial_y w & \partial_z w \end{bmatrix} = \begin{bmatrix} 0 & 0 & 0 \\ 0 & 0 & 0 \\ \partial_x w & \partial_y w & 0 \end{bmatrix}.$$

Thus,

$$\dot{p} = \dot{\theta} e_\theta + \dot{\varphi} \sin\theta e_\varphi \tag{1}$$

$$= (\text{I}_3 - pp^{\text{T}})[\nabla u_{\text{BG}} p]. \tag{2}$$

Using (1) and (2), we derive equations for $\dot{\theta}$ and $\dot{\varphi}$:

$$\begin{cases} \dot{\theta} = ([\nabla u_{\text{BG}} p] \cdot e_\theta) = -\sin^2\theta[\cos\varphi \partial_x w + \sin\varphi \partial_y w] \\ \dot{\varphi} = \frac{([\nabla u_{\text{BG}} p] \cdot e_\varphi)}{\sin\theta} = 0 \end{cases}$$

That is, the rod does not rotate along the z-axis. We combine these with equations for $\dot{x}$, $\dot{y}$, and $\dot{z}$, taking a propulsion velocity of 1, and obtain the following system of ODEs for unknown functions $x(t)$, $y(t)$, $z(t)$, $\theta(t)$, and $\varphi(t)$:

$$\begin{cases} \dot{x} = \cos\varphi \sin\theta \\ \dot{y} = \sin\varphi \sin\theta \\ \dot{z} = \cos\theta + w(x,y) \\ \dot{\theta} = -\sin^2\theta[\cos\varphi \partial_x w + \sin\varphi \partial_y w] \\ \dot{\varphi} = 0 \end{cases} \tag{3}$$

We then introduce a confinement: a channel whose surface is the impenetrable cylinder $x^2 + 2y^2 = 1$. Assuming a step size of 0.01, we let the numerical solution to the system above be the Euler scheme,

$$\mathcal{U}(n+1) = \mathcal{U}(n) + \Delta t \dot{\mathcal{U}}(n), \tag{4}$$

where $\mathcal{U}(n) = (x(n), y(n), z(n), \theta(n), \varphi(n))$. We adjust the rod location according to the cylinder by employing the following rule:

If $(x^{(n+1)})^2 + 2(y^{(n+1)})^2 > 1$, then use $\hat{x}^{(n+1)}$ and $\hat{y}^{(n+1)}$ for the next time step, such that

$$\hat{x}^{(n+1)} = d^{-1} x^{(n+1)},$$
$$\hat{y}^{(n+1)} = d^{-1} y^{(n+1)},$$
$$\text{where } d = \sqrt{(x^{(n+1)})^2 + 2(y^{(n+1)})^2 - 1}.$$

The listing below encodes the Euler scheme mentioned in (4) with functions derived from (3), while integrating the aforementioned collision rule and accounting for randomness. Notice that we re-parameterize the collision rule beginning in line 37 of Listing 1 according to the aspect ratio of the cylinder (i.e., a and b). In addition to the time and rod count variables, we also introduce rotational diffusion and flow rate as parameters. In the subsequent section, we present various figures and simulations that arise from implementing our numerical solution via the `for` loop below. Our results reflect Listing 1 unless otherwise stated.

Listing 1: Euler's scheme implemented in MATLAB

```matlab
1  N = 1000; % time
2  Delta = 0.01; % step size
3  D_rot = 0.01; % rotational diffusion
4  R = 1000; % rods
5  flow_rate = 0.1; global flow_rate;
6  % ellipsoidal parameters
7  a_ellipse = 2.0;  global a_ellipse;
8  b_ellipse = 1.0; global b_ellipse;
9
10 % Euler's scheme
11 for r=1:R
12     % initial conditions with randomness
13     r_x0 = a_ellipse * (2*rand()-1);
14     r_y0 = b_ellipse * (2*rand()-1);
15     while (r_x0^2/(a_ellipse^2) + r_y0^2/(b_ellipse^2) >= 1)
16         r_x0 = a_ellipse * (2*rand()-1);
17         r_y0 = b_ellipse * (2*rand()-1); end;
18     x0 = r_x0; y0 = r_y0; z0 = 0;
19     phi0 = 2*pi*rand();
20     theta0 = pi*rand();
21
22     x(1) = x0 + Delta*x_deriv(phi0, theta0);
23     y(1) = y0 + Delta*y_deriv(phi0, theta0);
24     z(1) = z0 + Delta*z_deriv(theta0, x0, y0);
25     theta(1) = theta0 + Delta*theta_deriv(theta0, phi0, x0, y0);
26     phi(1) = phi0 + Delta*0;
27
28     for n=2:N
29         r1=rand(); r2=rand();
30         x(n) = x(n-1) + Delta*x_deriv(phi(n-1), theta(n-1));
31         y(n) = y(n-1) + Delta*y_deriv(phi(n-1), theta(n-1));
32         z(n) = z(n-1) + Delta*z_deriv(theta(n-1), x(n-1), y(n-1));
33         theta(n) = theta(n-1) + Delta*theta_deriv(theta(n-1), phi(n-1), x(n-1), ...
34             y(n-1))+ sqrt(2*D_rot*Delta)*(2*r1-1);
34         phi(n) = phi(n-1) + Delta*0 + sqrt(2*D_rot*Delta)*(2*r2-1)/sin(theta(n-1));
35
36         % adjustment of trajectory due to confinement
37         if ((x(n))^2/(a_ellipse^2) + (y(n))^2/(b_ellipse^2) > 1)
38             d = sqrt((x(n))^2/(a_ellipse^2) + (y(n))^2/(b_ellipse^2));
39             x(n) = x(n)/d;
40             y(n) = y(n)/d;
41 end; end; end;
42
43 function z = x_deriv(phi, theta)
44     z = cos(phi) * sin(theta); end
45 function z = y_deriv(phi, theta)
46     z = sin(phi) * sin(theta); end
47 function z = z_deriv(theta, x, y)
48     global flow_rate; global a_ellipse; global b_ellipse;
49     z = cos(theta) + flow_rate*(x^2/(a_ellipse^2) + y^2/(b_ellipse^2) - 1); end
50 function z = theta_deriv(theta, phi, x, y)
51     global flow_rate; global a_ellipse; global b_ellipse;
52     z = -(sin(theta))^2 *(cos(phi)*(2*x/a_ellipse) + sin(phi)*(2*y/b_ellipse));
53     z = flow_rate * z; end
```

3 Results

We plot the end points of R rods for N time and indicate their final locations with red crosses (Figure 1). Moreover, we simulate trajectories for varying aspect ratios and flow rates, noting the subtle relationship between flow rate and rod accumulation, before generating a histogram representative of the density of rods throughout the cylinder. Whether we obtain a histogram solely from the final time N or from an array of rod locations compiled every 100th time n (Figure 2), we find that our observations do not point in favor of our initial hypothesis. Rather than accumulating at points of maximum curvature, it appears that rods accumulate at points of *minimum* curvature.
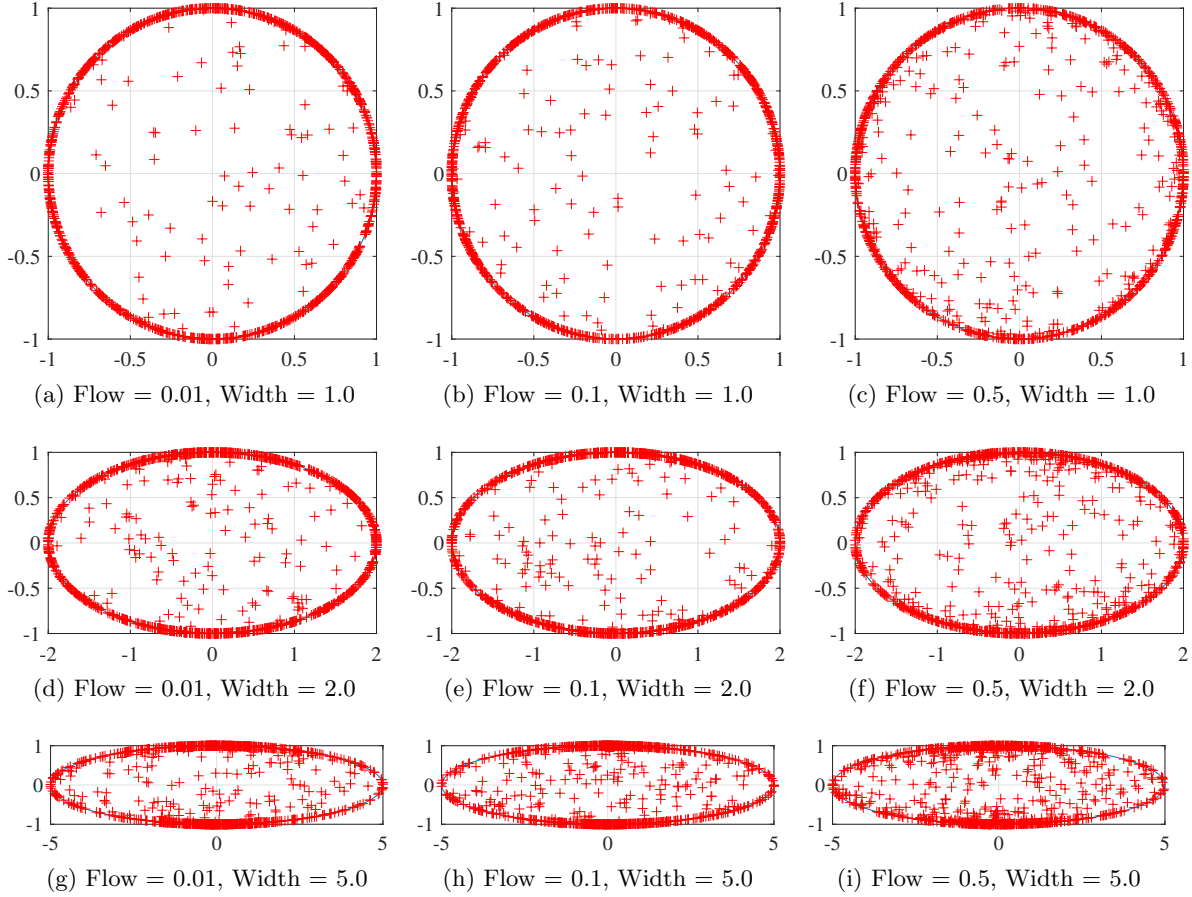

Figure 1: Final locations of rods plotted according to varying flow rates and aspect ratios.

This conclusion returns us to the introductory goal of determining whether or not it is possible to control active rod location and accumulation via the confinement curvature, while raising a new question: Is it possible to do the same via parameters aside from aspect ratio, such as rotational diffusion? We explore these notions by introducing variables N_a and N_b, which are $\frac{3}{4}$th of the cylinder's width and height, respectively, and which separate the ellipse into two disjoint areas. If the y coordinate of a rod is greater than N_b, it is counted into Area I, or the top-most quarter of the ellipse containing an accumulation of rods at minimum curvature. If its x coordinate is greater than N_a, it is counted into Area II, or the right-most quarter of the ellipse along the maximum

4

(a) Density of end locations at final time N

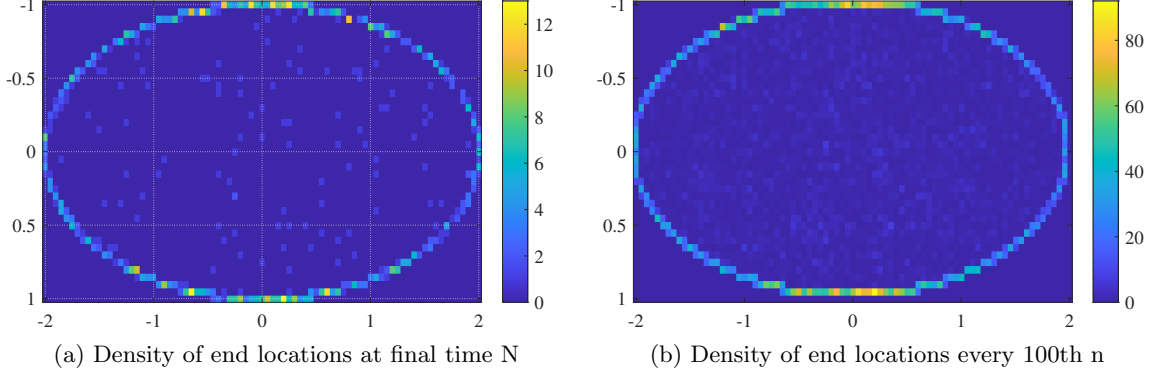(b) Density of end locations every 100th n

Figure 2: Histogram comparison of rod density simulated with flow = 0.1 and width = 2.0.

curvature. In so doing, we categorize rod locations from all times N and determine their average rod count (Figure 3). Notice that an aspect ratio of 1:1 yields a rod accumulation which converges to a limiting average of approximately 19% of the total rods along both the maximum and minimum curvatures, whereas an aspect ratio of 2:1 yields an accumulation of about 26% along the minimum curvature, nearly twice as much as that of the maximum curvature.

(a) Area I, aspect ratio 1:1

(b) Area II, aspect ratio 1:1

(c) Area I, aspect ratio 2:1

(d) Area II, aspect ratio 2:1

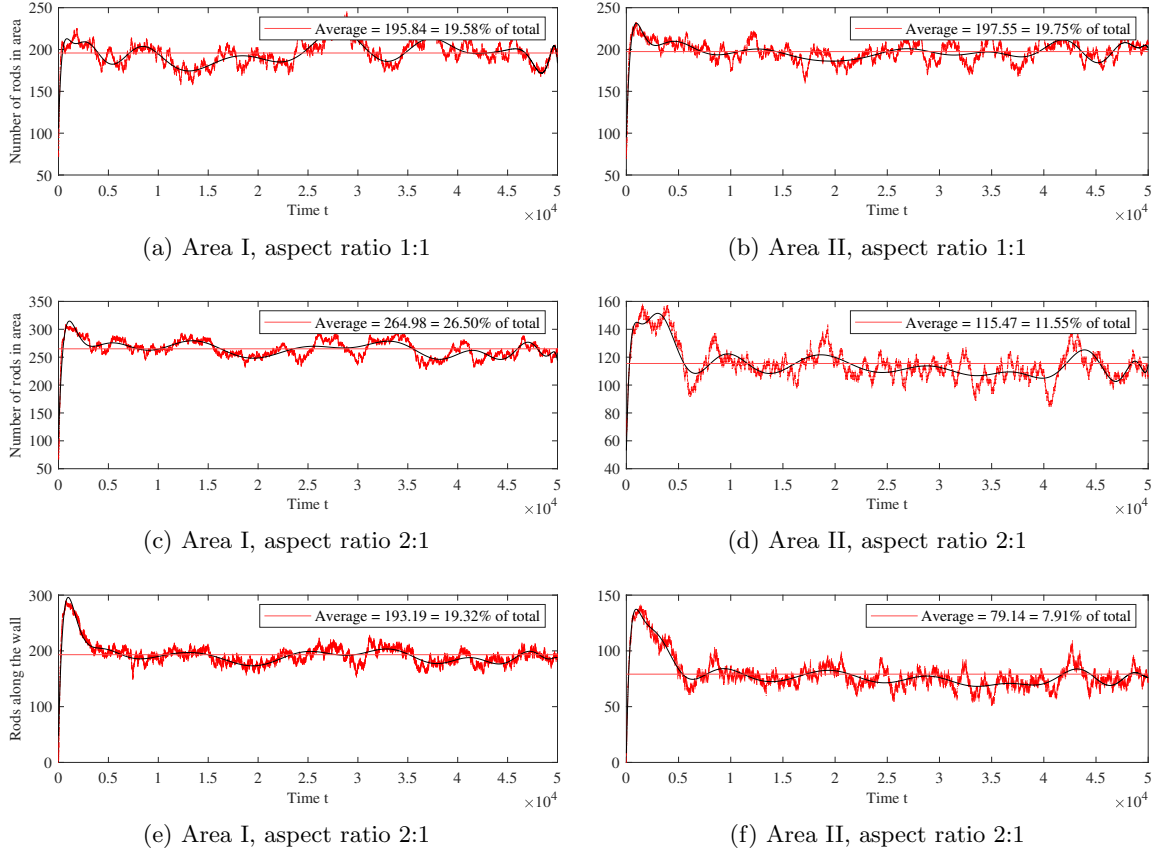(e) Area I, aspect ratio 2:1

(f) Area II, aspect ratio 2:1

Figure 3: Average rods in general (a)-(d) and along the walls (e)-(f) in Areas I and II.

Additionally, we compute the number of rods located along the confinement within Area I and Area II of a 2:1 cylinder, employing an error of 10^{-6} such that a rod is considered on the confinement if it is located within 10^{-6} of the confinement (Figure 3(e)-3(f)). Similar to our prior conclusion, we find that there is more than twice as many rods accumulated along the confinement of Area I than that of Area II.

Upon obtaining the average rod counts, we perform simulations with ranging values for aspect ratios, flow rate, rotational diffusion, and total rods. Below, we compare how the average percentage of rods among the two areas varies according to these four variables (Figure 4). Note that a roughly constant distribution among Figures 4(b)-4(d) suggest that the percentage of rods in areas I and II—or more generally, rod accumulation—is not significantly impacted by the flow rate, rotational diffusion, and total rods. The only correlation revealed among these four parameters is that between the percentage of rods and the confinement's aspect ratio (Figure 4(a)), as observed in Figure 1.

(a) Rod Accumulation in Areas vs. Aspect Ratio

(b) Rod Accumulation in Areas vs. Flow Rate

(c) Rod Accumulation in Areas vs. Rotational Diffusion

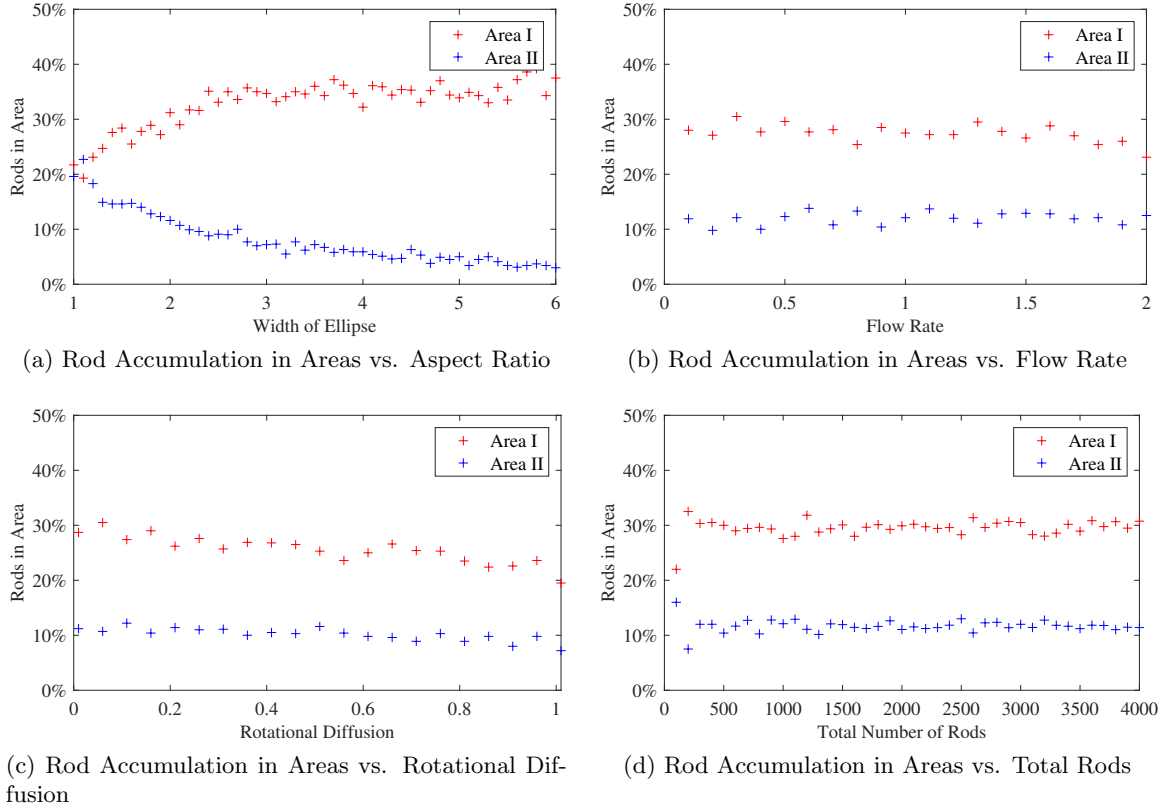(d) Rod Accumulation in Areas vs. Total Rods

Figure 4: Average rod counts in Areas I and II according to varying aspect ratio, flow rate, rotational diffusion, and total rods. Percentages refer to the ratio of average rods over the total rods. Unless rod count is being checked for dependence against the parameter, aspect ratio = 2:1 (i.e, width = 2.0), flow rate = 0.1, rotational diffusion = 0.01, and total rods = 1000. Time N is also decreased to 500 due to computing speed.

6

4 Discussion

Recall out initial hypothesis: Rods will tend to accumulate at points of maximum curvature, i.e., the two horizontal sides of the curve. In light of our results, we discuss why we reject this hypothesis in favor of the observation that rods accumulate at points of minimum curvature. By simulating and plotting the trajectories of rods with varying combinations of flow rate and aspect ratio, as well as obtaining a histogram of their accumulation, we find that rods do not accumulate at points of maximum curvature and rather do so at points of minimum curvature. In fact, when we varied three additional parameters—flow rate, rotational diffusion, and total number of rods—we determined that it is only the confinement's aspect ratio that is capable of altering the accumulation of rods at the minimum and maximum curvatures, such that, as the width of the ellipse increases, the rods accumulated along the area of minimum curvature increases, while those accumulated along the area of maximum curvature decreases.

One speculation is that this behavior is a result of the collision rule, which we briefly tested by altering it to the following rule: If $(x^{(n+1)})^2 + 2(y^{(n+1)})^2 > 1$, then use $\hat{x}^{(n+1)}$ and $\hat{y}^{(n+1)}$ for the next time step, such that $(\hat{x}^{(n+1)}, \hat{y}^{(n+1)})$ solves the following system:

$$\begin{cases} \dfrac{-b^2}{a^2} \cdot \dfrac{\hat{x}^{(n+1)}}{\hat{y}^{(n+1)}} = \dfrac{-(\hat{x}^{(n+1)} - x(n))}{\hat{y}^{(n+1)} - y(n)} \\ \dfrac{(\hat{x}^{(n+1)})^2}{a^2} + \dfrac{(\hat{y}^{(n+1)})^2}{b^2} = 1 \end{cases} \tag{5}$$

where a is the width and b is the height of the ellipse. Essentially, according to this new rule, if a point is found outside of the ellipse, we take a new point on the ellipse $(\hat{x}^{(n+1)}, \hat{y}^{(n+1)})$ such that the line that intersects the points $(x(n), y(n))$ and $(\hat{x}^{(n+1)}, \hat{y}^{(n+1)})$ is orthogonal to the tangent of the ellipse at $(\hat{x}^{(n+1)}, \hat{y}^{(n+1)})$. The first equation in the system accomplishes this by setting the slope of a tangent line on the ellipse equal to the negative reciprocal of a line that passes through a point outside of the ellipse and a point on the ellipse. The second equation checks that the point is in fact on the ellipse. We then take $(\hat{x}^{(n+1)}, \hat{y}^{(n+1)})$ for the next time step. Listing 2 implements this rule below and yields Figure 5.

Listing 2: New collision rule

```
1   if ((x(n))^2/(a_ellipse^2) + (y(n))^2/(b_ellipse^2) > 1)
2       syms x_new y_new
3       % set up system of equations [m1 m2]
4       % m1 sets the slope of the tangent line = negative reciprocal of slope of
5       % line that passes through (x(n),y(n)) and point on ellipse (x_new,y_new).
6       % m2 is the equation of the ellipse with (x_new,y_new) being a point
7       % on the ellipse.
8       m1 = (-(b_ellipse^2)/(a_ellipse^2))*(x_new/y_new) == -(x_new - x(n))/(y_new ...
            - y(n));
9       m2 = ((x_new^2)/(a_ellipse^2)) + ((y_new^2)/(b_ellipse^2)) == 1;
10      m = [m1 m2];
11
12      % use vpasolve to solve the system above for x_new and y_new.
13      v = vpasolve(m, [x_new y_new], [-a_ellipse, a_ellipse]);
14
15      % it returns 4 solutions, including complex solutions, so we
```

```
16      % choose the min real solution.
17      for k=1:4
18          x_candidate(k) = real(v.x_new(k));
19          y_candidate(k) = real(v.y_new(k));
20          imaginary_part = imag(v.x_new(k))^2 + imag(v.y_new(k))^2;
21          if (imaginary_part>0.00001)
22              d(k) = 2022;
23          else
24              d(k) = (x(n)-x_candidate(k))^2 + (y(n)-y_candidate(k))^2;
25          end; end;
26      [d_min, k_min] = min(d);
27      x(n) = v.x_new(k_min);
28      y(n) = v.y_new(k_min);
29  end;
```

We supposed that discrepancies among collision rules are absorbed by randomness, which would lead us to believe that the collision rule *will not* impact the rod distribution; hence, rod accumulation will still exhibit a propensity towards minimum curvature. However, we see in Figure 5 that upon implementation of the new collision rule, active rods subtly accumulate along the maximum curvature, which calls into question the accuracy of our initial collision rule. Altogether, a future study is suggested in order to further investigate the reason behind the rods' tendency to accumulate at points of either minimum or maximum curvature.

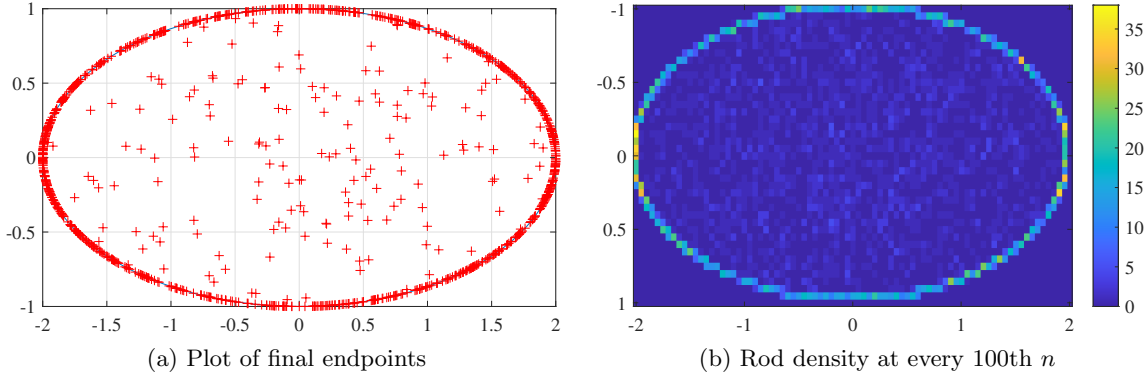(a) Plot of final endpoints   (b) Rod density at every 100th n

Figure 5: Simulations of 1000 rods with $N = 500$ implementing new collision rule.

Nevertheless, the analysis of clustering through the active rod model, such as that observed in our study, is considered crucial to the understanding of the morphodynamics of clustering and colonization [3]. For instance, a previous study by Zachreson *et al.* employed specific parameters that reflected their experimental system in an attempt to understand the behavior of motile rod-shaped cells of *P. aeruginosa* growing on agar [6, 7]. Although the scope of Zachreson's study is more narrowed according to their experimental system and fails to account for confinement, a separate study by Figueroa-Morales *et al.* introduces microfluidic channels to E. coli transport and analyzes how their upstream migration relates to the channels' flow rates [2]. In this context, our project has the potential to help develop an efficient method for clearing medical tubes of infectious bacteria polluting its walls. Perhaps isolating the accumulation of the system of bacteria via altering the channel's aspect ratio will be a first step in the solution. With applications within and beyond

medicine and materials science, the results here suggest future theoretical and experimental avenues for exploring the role played by the active rod model in these biological phenomena.

References

[1] M. Bär, R. Großmann, S. Heidenreich, and F. Peruani. Self-propelled rods: Insights and perspectives for active matter. *Annual Review of Condensed Matter Physics*, 11(1):441–466, mar 2020.

[2] N. Figueroa-Morales, G. Leonardo Miño, A. Rivera, R. Caballero, E. Clément, E. Altshuler, and A. Lindner. Living on the edge: transfer and traffic of e. coli in a confined flow. *Soft Matter*, 11:6284–6293, 2015.

[3] M. Imaran, M. Inamdar, R. Prabhakar, and R. Chelakkot. Cluster and conquer: The morpho-dynamics of invasion of a compliant substrate by active rods, 2021.

[4] M. Potomkin, A. Kaiser, L. Berlyand, and I. Aranson. Focusing of active particles in a converging flow. *New Journal of Physics*, 19(11):115005, nov 2017.

[5] L. D. Rubio, M. Potomkin, R. D. Baker, A. Sen, L. Berlyand, and I. S. Aranson. Self-propulsion and shear flow align active particles in nozzles and channels. *Advanced Intelligent Systems*, 3(2):2000178, 2021.

[6] C. Zachreson, C. Wolff, C. Whitchurch, and M. Toth. Emergent pattern formation in an interstitial biofilm. *Physical Review E*, 95, 11 2016.

[7] C. Zachreson, X. Yap, E. S. Gloag, R. Shimoni, C. B. Whitchurch, and M. Toth. Network patterns in exponentially growing two-dimensional biofilms. *Phys. Rev. E*, 96:042401, Oct 2017.